An improved coarse-grained model of solvation and the hydrophobic effect

Patrick Varilly,[1] Amish J. Patel,[1] and David Chandler[1, a]

Department of Chemistry, University of California, Berkeley, California 94720

We present a coarse-grained lattice model of solvation thermodynamics and the hydrophobic effect that implements the ideas of Lum-Chandler-Weeks (LCW) theory [J. Phys. Chem. B **103**, 4570 (1999)] and improves upon previous lattice models based on it. Through comparison with molecular simulation, we show that our model captures the length-scale and curvature dependence of solvation free energies with near-quantitative accuracy and two to three orders of magnitude less computational effort, and further, correctly describes the large but rare solvent fluctuations that are involved in dewetting, vapor tube formation and hydrophobic assembly. Our model is intermediate in detail and complexity between implicit-solvent models and explicit-water simulations.

I. INTRODUCTION

This is a technical paper that addresses how the hydrophobic effect may be understood quantitatively. Despite its technical nature, the physical ideas and final model we formulate should be accessible and potentially interesting to a wide audience of researchers who are confronted with the many manifestations of the hydrophobic effect, and are in need of an effective quantitative tool for treating them.

The hydrophobic effect is presumed to be an important driving force in biology and nanoscale self-assembly.[1–3] Because of its collective nature and its length-scale dependence,[4] and because of its nonlocal dependence on solute surface moeities,[5–7] modeling the hydrophobic effect remains a challenge. To treat it theoretically, one could track the explicit position of possibly tens of thousands of water molecules around solutes of interest,[8,9] but the computational cost of this approach limits its applications. Alternatively, at significantly reduced cost, one could replace explicit waters by an implicit solvent model, as is done in the generalized Born and surface area (GBSA) approach.[10,11] In this paper, building on previous efforts,[12–14] we propose a coarse-grained model intermediate in detail between these two extremes, one that retains most of the computational advantage of implicit solvent models and overcomes two of their significant conceptual flaws: their incorrect scaling behavior and their neglect of rare but large solvent density fluctuations that play pivotal roles in the dynamics of assembly.

Solvation free energies[15,16] of solutes with sub-nanometer features, exactly the size prevalent in biological regimes, do not in general[17] scale as surface area.[12,19,20] By construction, models that assume such scaling significantly underestimate the driving force for hydrophobic assembly.[4,21] Our model, on the other hand, captures the correct scaling behavior with solute size for generic solute geometries.

Since hydrophobicity is a solvent property as much as it is a solute property, it is important to consider the solvent on length scales dictated by the solute(s). Numerous studies of hydrophobicity[4,14,22–32] have shown that rare solvent motions and dewetting transitions in confining environments play a critical role in solute assembly and function. Our model adequately captures these rare and important fluctuations. To demonstrate this, we consider the water number distribution $P_V(N)$ in a probe volume V. Hummer et al. introduced the idea of characterizing this distribution in the context of solvation theory,[33] and the utility of this function has been demonstrated subsequently.[34]

The GBSA model,[10,11] widely used in biological settings, captures the effect of electrostatics with reasonable accuracy, but its treatment of the hydrophobic effect is less adequate,[20,37–39] for the reasons discussed above. Interesting examples of solutes for which hydrophobicity is essential, and for which GBSA is unsuitable, include large classes of proteins, such as those involved in transmembrane protein recognition and insertion,[40] and versatile chaperones.[41] It is these kinds of solutes for which our approach may eventually prove most useful.

The ideas behind our model are those of Lum-Chandler-Weeks (LCW)[12] theory. Ten Wolde, Sun and Chandler[13,14] generalized this theory by casting it in terms of a Hamiltonian for a lattice field theory. The motivation for that development was to facilitate treatments of large length scale dynamics. The motivation of the current work is similar, though in this paper we confine our attention to time-independent properties. The main contribution of this paper is to improve upon these previous attempts, and to introduce concrete implementations of the underlying theory that illustrate the improvements, which are significant.

The paper is organized as follows. In Section II, we sketch the physical ideas behind our model and present their implementation in a tractable format. The derivation and approximations made therein are left to the Appendix. In Section III, we consider the accuracy of our model by computing the solvation free energies of solutes and $P_V(N)$ distributions for various geometries, with and without adhesive solute-solvent interactions. Finally, in Section IV we conclude with a discussion of the merits and limitations of the present implementation of the

a) Electronic mail: chandler@berkeley.edu

model.

II. MODEL

A. Density fields and Hamiltonian

In this section we first consider general features of a liquid solvent, specializing to water only later. We focus on the solvent density, $\rho(\mathbf{r})$. For water in particular, $\rho(\mathbf{r})$ refers to the instantaneous positions of water oxygen atoms. Effects of other variables such as molecular orientations appear implicitly in terms of parameters. We decompose density into large and small length-scale contributions $\rho_\ell n(\mathbf{r})$ and $\delta\rho(\mathbf{r})$, respectively,

$$\rho(\mathbf{r}) = \rho_\ell n(\mathbf{r}) + \delta\rho(\mathbf{r}). \tag{1}$$

Here, ρ_ℓ is the bulk liquid density, and $n(\mathbf{r})$ is an Ising-like field that is 1 in regions that are locally liquid-like and 0 in regions that are locally vapor-like. The field takes on intermediate values only around interfacial regions. This large length-scale field describes extended liquid-vapor interfaces, while the small length-scale field describes more rapidly-varying density fluctuations. This separation implies some form of space-time coarse-graining to define $n(\mathbf{r})$, a coarse-graining which is most reasonable for dense fluids far from their critical points. The key development of LCW was to describe how to (a) perform this decomposition, and (b) couple the two separate fields.

Building on the work of ten Wolde, Sun and Chandler,[13] we construct a Hamiltonian for the solvent density that captures the dominant physics. We have

$$H[n(\mathbf{r}), \delta\rho(\mathbf{r})] = H_{\text{large}}[n(\mathbf{r})]$$
$$+ H_{\text{small}}[\delta\rho(\mathbf{r}); n(\mathbf{r})] + H_{\text{int}}[n(\mathbf{r}), \delta\rho(\mathbf{r})]. \tag{2}$$

The term $H_{\text{large}}[n(\mathbf{r})]$ captures the physics of interface formation in $n(\mathbf{r})$. For the term $H_{\text{small}}[\delta\rho(\mathbf{r}); n(\mathbf{r})]$, we exploit the observation that small length-scale density fluctuations in homogeneous liquids obey Gaussian statistics.[33,42,43] Thus, for a given configuration of $n(\mathbf{r})$, we assume that $\delta\rho(\mathbf{r})$ has Gaussian statistics with variance

$$\chi(\mathbf{r}, \mathbf{r}'; [n(\mathbf{r})]) = \langle \delta\rho(\mathbf{r})\delta\rho(\mathbf{r}')\rangle_{n(\mathbf{r})}.$$

Here, the right-hand side denotes the thermal average of $\delta\rho(\mathbf{r})\delta\rho(\mathbf{r}')$ under the constraint of fixed $n(\mathbf{r})$. The term $H_{\text{small}}[\delta\rho(\mathbf{r}); n(\mathbf{r})]$ is then a Gaussian with this variance, namely

$$H_{\text{small}}[\delta\rho(\mathbf{r}); n(\mathbf{r})] =$$
$$\frac{k_{\text{B}}T}{2} \int_{\mathbf{r}} \int_{\mathbf{r}'} \delta\rho(\mathbf{r})\chi^{-1}(\mathbf{r}, \mathbf{r}'; [n(\mathbf{r})])\delta\rho(\mathbf{r}'), \tag{3}$$

where $k_{\text{B}}T$ is temperature, T, times Boltzmann's constant. For conciseness, we use an abbreviated integration notation, where the integration variable is denoted with a subscript to the integral sign, and the integration domain is all of space unless otherwise stated. We approximate the variance with

$$\chi(\mathbf{r}, \mathbf{r}'; [n(\mathbf{r})]) \approx \begin{cases} \chi_0(\mathbf{r} - \mathbf{r}'), & n(\mathbf{r}) = n(\mathbf{r}') = 1; \\ 0, & \text{otherwise,} \end{cases} \tag{4}$$

where $\chi_0(\mathbf{r})$ can be written in terms of the radial distribution function $g(r)$ as

$$\chi_0(\mathbf{r}) = \rho_\ell \delta(\mathbf{r}) + \rho_\ell^2 [g(|\mathbf{r}|) - 1]. \tag{5}$$

For the uses we make of the approximation in Equation (4), corrections have quantitative but not qualitative effects, as discussed in the Appendix and also Ref. 44. Finally, $H_{\text{int}}[n(\mathbf{r}), \delta\rho(\mathbf{r})]$ is an effective coupling between $n(\mathbf{r})$ and $\delta\rho(\mathbf{r})$ due to unbalanced attractive forces in the solvent, whose details are given in the Appendix.

In the absence of large solutes, fluctuations in $n(\mathbf{r})$ are unlikely. The only fluctuations of significance in that case are those described by $\delta\rho(\mathbf{r})$. In the presence of large solutes, however, $n(\mathbf{r})$ will often differ significantly from its bulk mean value. In that case the statistics of $\delta\rho(\mathbf{r})$ is modified and the coupling $H_{\text{int}}[n(\mathbf{r}), \delta\rho(\mathbf{r})]$ between $n(\mathbf{r})$ and $\delta\rho(\mathbf{r})$ becomes significant. When $\delta\rho(\mathbf{r})$ is integrated out, a renormalized Hamiltonian for $n(\mathbf{r})$ results.

LCW theory[12] is a mean-field theory for the average large length-scale field, $\langle n(\mathbf{r})\rangle$, so it ignores the effects of large-scale fluctuations in $n(\mathbf{r})$. Subsequent lattice implementations of LCW theory[13,14,45] have incorporated fluctuations in the simplest possible manner. The present model refines these previous attempts to achieve near-quantitative accuracy for solvation free-energies and correct behavior of fluctuations in $n(\mathbf{r})$. Most importantly, we improve the calculation of the interfacial energies due to $n(\mathbf{r})$.

To write down the renormalized Hamiltonian, we begin by describing $n(\mathbf{r})$ with reference to a cubic grid of spacing λ, depicted in Figure 1, and we denote its value at the center of cell i by n_i. Then, $n(\mathbf{r})$ is given by

$$n(\mathbf{r}) = \sum_i n_i \Psi(\mathbf{r} - \mathbf{r}_i), \tag{6}$$

where $\mathbf{r}_i$ is the center of cell i and n_i is 1 or 0, and the sum is over all cells i. The function $\Psi(\mathbf{r})$ is maximal with value 1 at $\mathbf{r} = \mathbf{0}$; it is cubic symmetric about the origin; and it is zero when the magnitude of any of the Cartesian components of $\mathbf{r}$ is greater than λ. The value of λ, about which we will say more later, should be roughly the size of the bulk correlation length of the liquid solvent. The typical size of interfacial energies between cells on this grid is $\gamma\lambda^2$, where γ is the liquid-vapor surface tension of the solvent. The dissolved solute excludes solvent density from a volume v, and we define $\bar{v}$ to be its complement, so that the total volume of the system is the union of v and $\bar{v}$. The excluded volume can be of any
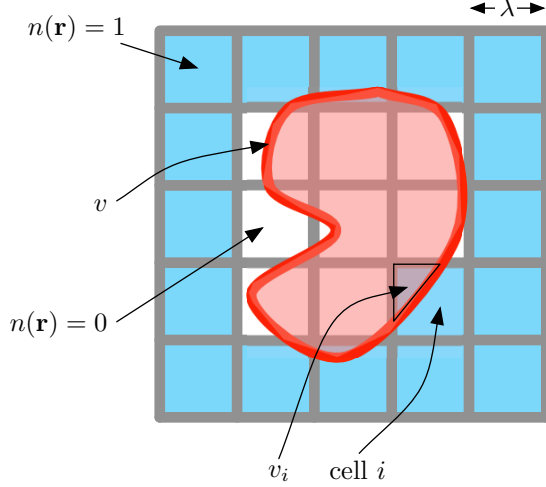
FIG. 1. Schematic showing the solute and the large length-scale density field on a grid

shape, and it can be composed of disconnected parts. In Ref. 42, regions within v are called "in", and regions within $\bar{v}$ are called "out". For any volume V, we have the projector $b_V(\mathbf{r})$,

$$b_V(\mathbf{r}) = \begin{cases} 1, & \mathbf{r} \in V, \\ 0, & \text{otherwise,} \end{cases} \quad (7)$$

so that $b_V(\mathbf{r}) + b_{\bar{V}}(\mathbf{r}) = 1$. We denote the overlap of v or $\bar{v}$ with cell i by v_i and $\bar{v}_i$, respectively.

In the absence of a solute, the Gaussian nature of $\delta\rho(\mathbf{r})$ results in solvent number fluctuation correlations. The correlations between the portions of cells i and j that overlap with two volumes V and V', respectively, form the elements of a matrix

$$\chi_{ij}(V, V') = \int_{\mathbf{r} \in i} \int_{\mathbf{r}' \in j} b_V(\mathbf{r})\chi_0(\mathbf{r}, \mathbf{r}')b_{V'}(\mathbf{r}'). \quad (8)$$

Here, the domain of the $\mathbf{r}$ and $\mathbf{r}'$ integrals are restricted to the volume of cells i and j, as indicated. A way to estimate these elements is outlined in the Appendix. The resulting matrix is used to calculate entropic effects due to solvent exclusion and the linear response of solvent density to external fields.

Part of the renormalized Hamiltonian is the free energy $H_{\text{large}}[n(\mathbf{r})]$ of the field $n(\mathbf{r})$ in the absence of external solutes. We estimate this contribution using a Landau-Ginzburg Hamiltonian

$$H_{\text{large}}[n(\mathbf{r})] = \int_{\mathbf{r}} \left[w(n(\mathbf{r}), \mu) + \frac{m}{2}|\nabla n(\mathbf{r})|^2 \right], \quad (9)$$

where $w(\rho/\rho_\ell, \mu)$ is the grand free energy density for the liquid solvent at a given density, ρ, and chemical potential, μ, relative to that of the gas. The parameter m reflects surface tension and intrinsic interfacial width. At

liquid-gas phase coexistence, $\mu = 0$, the value of the integral is conveniently expressed as the sum $\gamma\lambda^2 \sum_i h_i$ with the local integrals

$$h_i = \frac{1}{\gamma\lambda^2} \int_{x_i}^{x_i+\lambda} dx \int_{y_i}^{y_i+\lambda} dy \int_{z_i}^{z_i+\lambda} dz$$
$$\left[w(n(x, y, z), 0) + \frac{m}{2}|\nabla n(x, y, z)|^2 \right]. \quad (10)$$

The quantity h_i depends only on the values of n_j for cells j that share one of the corners of cell i. There are only 14 distinct possible values of h_i, which can be precalculated numerically for a given free energy density $w(n, 0)$ and cell size λ, as detailed in the Appendix. In previous modeling, the simpler Ising model estimate $\gamma\lambda^2 \sum_{\langle ij \rangle}(n_i - n_j)^2$ has been used. For reasons discussed in the Appendix, this simpler estimate proves less accurate than the one used here.

With the above notation, we now write the Hamiltonian for our model, which constitutes the main result of the paper,

$$H_{\text{eff}}[\{n_i\}] = \gamma\lambda^2 \sum_i h_i - \mu\rho_\ell\lambda^3 \sum_i n_i$$
$$+ K \sum_i \phi_i(-\rho_\ell n_i v_i)$$
$$+ k_{\text{B}}T[\langle N \rangle_v^2/2\sigma_v + C/2], \quad (11a)$$

where

$$\phi_i = 2a\rho_\ell \left[1 - \frac{1}{2}n_i - \frac{1}{12}\sideset{}{'}\sum_{j\,(\text{nn}i)} n_j \right], \quad (11b)$$

$$\langle N \rangle_v = \rho_\ell \sum_i n_i v_i, \quad (11c)$$

$$\sigma_v = \sum_{i,j} n_i \chi_{ij}(v, v) n_j, \quad (11d)$$

$$C = \begin{cases} \ln(2\pi\sigma_v), & \langle N \rangle_v > 1, \\ \max[\ln(2\pi\sigma_v), \langle N \rangle_v], & \text{otherwise.} \end{cases} \quad (11e)$$

The field ϕ_i, with strength governed by the positive parameter a, is what Weeks has termed an "unbalancing potential".[46–50] The primed sum over $j(\text{nn}i)$ is a sum over the six cells j that are nearest neighbors to cell i. The final expression for ϕ_i shown above, with renormalization constant K, is the result of an accurate and computationally convenient approximation, which is described in detail in the Appendix.

The terms on the right-hand-side of Equation (11a) respectively approximate: the free-energy cost of establishing interfaces in $n(\mathbf{r})$, the pressure-induced bias towards the liquid phase, the effective coupling between $n(\mathbf{r})$ and $\delta\rho(\mathbf{r})$ induced by the presence of a solute, and the entropic cost of excluding solvent density from the portions of v where $n(\mathbf{r}) = 1$. As the total number of waters to be excluded, $\langle N \rangle_v$, approaches zero, the statistics of solvent number fluctuations in v changes from Gaussian to Poisson, so that its variance, σ_v, also approaches

zero. Equation (11e) captures this change continuously and prevents $H_{\text{eff}}[\{n_i\}]$ from becoming infinitely negative in this limit.

B. Incorporating Solute-solvent attractions

The above Hamiltonian pertains to the simplest case, where the solute interacts with the solvent only by hard-core repulsion. Realistic solutes additionally have attractive interactions with the solvent that can be modeled as an external potential $u(\mathbf{r})$ that couples to $\rho(\mathbf{r})$. Such a potential induces an additional term in our Hamiltonian, which we denote by $H_u[\{n_i\}]$. To describe this term, we define a discretized analogue u_i of $u(\mathbf{r})$,

$$u_i = \frac{1}{\bar{v}_i} \int_{\mathbf{r} \in i} b_{\bar{v}}(\mathbf{r}) u(\mathbf{r}). \quad (12)$$

Notice that u_i is independent of $u(\mathbf{r})$ for values of $\mathbf{r}$ inside the solute. The apparent divergence, where v completely overlaps cell i, has no effect in the final expression. In particular,

$$
\begin{aligned}
H_u[\{n_i\}] = & \\
& \sum_i u_i n_i \Big[\rho_\ell \bar{v}_i - \sum_j \chi_{ij}(\bar{v}, v) n_j \langle N \rangle_v / \sigma_v \\
& \quad - \sum_j \chi_{ij}(\bar{v}, \bar{v}) n_j \beta (u_j + \phi_j) \Big] \\
& \quad + \frac{k_{\text{B}} T}{2} \sum_{i,j} \beta u_i n_i \chi_{ij}(\bar{v}, \bar{v}) n_j \beta u_j, \quad (13)
\end{aligned}
$$

where β is the reciprocal of $k_{\text{B}}T$. The first part is the mean-field contribution $\int_{\mathbf{r}} u(\mathbf{r}) \langle \rho(\mathbf{r}) \rangle$, while the last term is the entropic cost of the external potential modifying the average solvent density in the vicinity of the solute.

C. Parameters of the Hamiltonian

We now specialize our model to water at ambient conditions, $T = 298\,\text{K}$ and 1 atm pressure, p. Further, we comment upon what changes are required for applications at different states of water.

The cell size length λ should be no smaller than the intrinsic width of the liquid-vapor interface. Based upon the interfacial profile of the SPC/E model,[19,51] we therefore pick $\lambda = 4\,\text{Å}$. This is the minimal scale over which the time-averaged solvent density can transition from liquid-like to vapor-like values. Following Ref. 52, we use the free-energy density

$$w(n, \mu) = \frac{2m}{d^2}(n-1)^2 n^2 - \mu \rho_\ell n, \quad (14)$$

with $d = 1.27\,\text{Å}$ because this choice reproduces the sigmoidal density profile of water-vapor interfaces at coexistence. The resulting values of h_i are tabulated in the Appendix. The bulk liquid density ρ_ℓ is the experimental value,[53] whereby a liquid cell contains $\rho_\ell \lambda^3 \approx 2.13$ waters on average. The value of m is chosen such that the interfacial energy of vapor spheres of radius R tends to $4\pi\gamma R^2$ for large R. At ambient conditions, the experimental value for the surface tension[53] yields $\gamma \lambda^2 \approx 2.80\,k_{\text{B}}T$. Finally, the relative chemical potential is given by $\mu \approx (p - p_{\text{vap}})/\rho_\ell$, where p_{vap} is the vapor pressure at 298 K. This relationship gives $\mu \approx 7.16 \times 10^{-4}\,k_{\text{B}}T$, which is quite small, reflecting that water at ambient conditions is nearly at coexistence with its vapor.

The matrix elements $\chi_{ij}(V, V')$ are computed from the radial distribution function, $g(r)$, and we derive this function from Narten and Levy's tabulated data.[54] It is a convenient data set because it covers a broad range of temperatures for the liquid at and near $p = 1\,\text{atm}$. At one temperature, 25°C, we have checked that a different estimate of the radial distribution function, that of the SPC/E model, yields similar matrix elements, and the resulting solvation properties are essentially identical to those obtained when the $\chi_{ij}(V, V')$'s are computed from the Narten-Levy data at the same temperature.

The only parameters that we estimate through fitting are the strength a of the unbalancing potential and the renormalization constant K. In the absence of solute-solvent attractions, only the product of a and K is relevant. Values of a and K with $Ka\rho_\ell = 2.1\,k_{\text{B}}T$ allow us to match the solvation free energies of hard spheres in SPC/E water (see below). By comparing the average value of the computationally convenient approximate expression involving ϕ_i in Equation (11a) with that of its complete and unrenormalized counterpart, as is done in the Appendix, we find that K is about 1/2, so that $a\rho_\ell \approx 4.2\,k_{\text{B}}T$. This value for a is close to the original LCW estimate,[12] arrived at from a different criterion.

These values are applicable at ambient conditions. As temperature and pressure vary, only γ, μ and $g(r)$ vary appreciably, while K varies slightly. In particular, surface tension decreases roughly linearly with temperature[53] (with $d\gamma/dT \approx -0.15\,\text{mJ/m}^2\cdot\text{K}$ which is $-5.8 \times 10^{-3}\,k_{\text{B}}T/\lambda^2\cdot\text{K}$ at $T = 298\,\text{K}$). As noted above, μ increases roughly linearly with pressure. The pair correlation function $g(r)$ loses some structure for temperatures above 50 °C. The terms that are modeled by the renormalization constant K reflect the degree to which solvent density layers next to a solute. Since this layering reflects the structure of $g(r)$, we expect K to be slightly state-dependent, with its value increasing with temperature.

Conversely, liquid water has a nearly constant density and bulk correlation length at the temperatures and pressures where our model would be useful, so ρ_ℓ and λ can be taken as constant as well. Theoretical estimates for a in simple liquids (Eq. 4 in Ref 46) are state-independent, so we expect that in water, a will be nearly state-independent as well.[55]

III. APPLICATIONS AND RESULTS

A. Solvation Free Energies

To test our model's ability to capture the length-scale dependence of solvation, and to parametrize the strength of the unbalancing potential, we have calculated the solvation free energy of hard spheres of different radii. Whether within our model or using explicit water simulations, we calculate the solvation free energy of a solute following the guidelines of Ref. 56. Briefly, we first define a series of $M+1$ solutes S_0 through S_M that slowly interpolate from an empty system (S_0) to the final solute of interest (S_M). We then sequentially calculate the free energy difference between solute m and solute $m+1$ using the Bennett acceptance ratio estimator[57] (BAR), and, where necessary, the linear interpolation stratification procedure of Ref. 56. Error estimates are calculated using BAR, and are generally smaller than 0.5%.

Our model (Equation (11a)) involves only simple arithmetic, so free energies can be calculated with little computational effort. For example, calculating the solvation free energy of hard spheres of up to $14\,\text{Å}$ in radius in increments of $0.5\,\text{Å}$ (Figure 2) takes about 1 hour on a single 2 GHz machine with a code that has not been fully optimized, whereas a similar calculation in explicit SPC/E waters with GROMACS[58] would take around 600 hours on the same machine to obtain a similar statistical accuracy.

Hard-sphere solvation free energies scale as solute volume for small spheres, and as surface area for large spheres, with a smooth crossover at intermediate sizes.[4] Figure 2 illustrates this behavior and compares the results of our model to previous simulation results using SPC/E water.[19] As the model manifestly reproduces the small- and large-length scale limits, the most significant feature illustrated in Figure 2 is the *gradual* crossover from volume to surface area scaling. Ignoring the unbalancing potential leads to a qualitatively correct scaling behavior. However, adjustment of the single parameter a, which determines the strength of the unbalancing potential, yields a near-exact agreement between our model and the SPC/E results for all sphere sizes. In all subsequent results, the parameter a is fixed at this value.

The model results have small lattice artifacts—results that depend upon the position of the solute relative to that of the coarse-grained lattice—as shown in the inset of Figure 2. When studying stationary solutes, lattice artifacts may be mitigated by performing multiple calculations, differing only by small displacements of the solutes, and then averaging the results. When studying dynamical phenomena, lattice artifacts tend to pin solutes into alignment with the coarse-grained lattice. For arbitrary molecular solutes, we expect that pinning forces acting on one portion of the molecule will generically oppose pinning forces on other parts of the molecule, so that the total pinning forces will largely cancel out. However, when treating many identical molecules, lattice artifacts
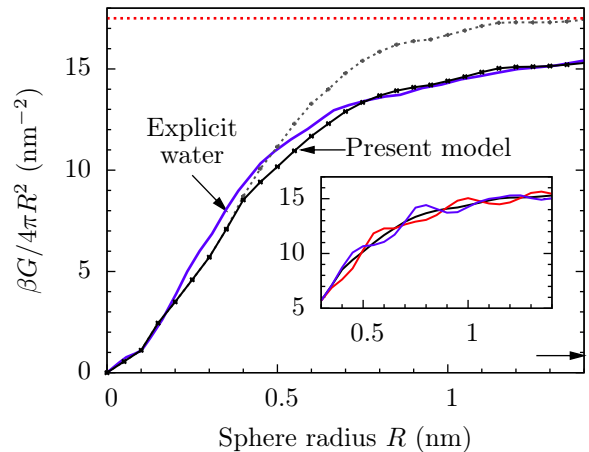

FIG. 2. Solvation free energies G of hard spheres of increasing radii, as calculated from explicit SPC/E water simulations[19] (solid blue), from the coarse-grained model (solid black), and from the most common GBSA variant[60] (arrow at bottom right). When the coarse-grained model has no unbalancing potential ($a = 0$, dashed gray), the intermediate-size regime is only qualitatively reproduced. For large spheres, the ratio of G to surface area tends to the liquid-vapor surface tension γ (horizontal red dots). Inset: Illustration of lattice artifacts. The spheres are centered at different offsets from the lattice: a generic position $(0.98\,\text{Å}, 0.79\,\text{Å}, 1.89\,\text{Å})$ that breaks all rotational and mirror symmetries (black), a lattice cell corner (blue) and a lattice cell center (red). All three curves are identical for $R \leq 0.35\,\text{nm}$.

can add constructively, and additional steps are needed to mitigate them.[59]

Since the unbalancing potential is explicitly parametrized with the solvation free energy of hard spheres, it is useful to evaluate the accuracy of the results in other geometries. To this effect we computed the solvation free energies of a family of hexagonal plates, consisting of 37 methane-like oily sites arranged into three concentric rings. We control the size of these plates, depicted in Figure 3, by varying the distance d between neighboring oily sites. For our calculations with explicit SPC/E water, the sites are uncharged and interact with the solvent molecules via a standard[62] water-methane Lennard-Jones potential. To study the role of attractive interactions, we split this Lennard-Jones potential using the Weeks-Chandler-Andersen (WCA) prescription[64] into a repulsive part $u_0(r)$ and an attractive part $\Delta u(r)$. The magnitude of the attractive tail can be varied systematically with a scaling parameter η, such that

$$u_\eta(r) = u_0(r) + \eta\Delta u(r). \qquad (15)$$

For the ideal hydrophobic plate, we set η to zero.

In the coarse-grained model, the repulsive core of the solute is represented as an excluded volume. To construct it, we replace each solute particle by a thermally-
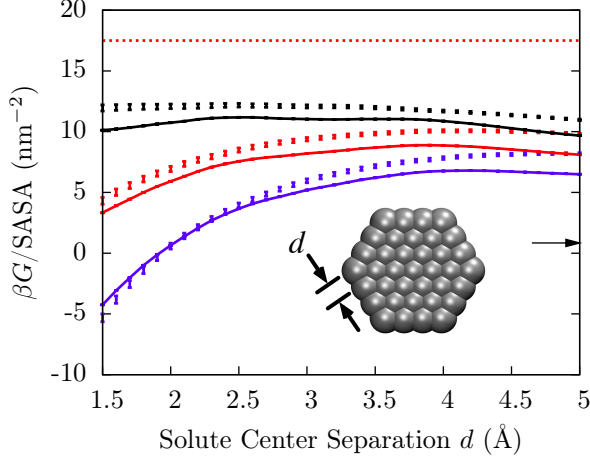
FIG. 3. Solvation free energies G of hexagonal plates, as a function of plate size, as calculated by the coarse-grained model (solid lines), by explicit SPC/E water simulations (points), and by the most common GBSA variant (arrow on right). Three values of the attractive interaction strength η are shown: 0.0 (black), 0.5 (red) and 1.0 (blue). Solvent-accessible surface areas (SASAs) were calculated using VMD,[61] with a particle radius of 1.97 Å, a solvent radius of 1.4 Å, and 1,000,000 samples per atom. The bulk liquid-vapor surface tension of water (horizontal red dots) is shown. Inset: Detail of the hexagonal plate. The solvent-excluded volume of each oily site is a sphere of radius $R_0 = 3.37$ Å.

equivalent hard sphere, whose radius R_0 is estimated according to

$$R_0 = \int_0^\infty dr\, [1 - \exp(-\beta u_0(r))],$$

which is a first approximation to the WCA value of this radius,[65,66] and is essentially the radius at which $u_0(r)$ is $k_B T$. The excluded volume is then the union of the hard-sphere volumes of each solute site.

Figure 3 compares the solvation free energies for this family of solute plates computed from our atomistic simulations with those computed from the coarse-grained model with the unbalancing parameter a determined above for solvated hard spheres. Now, with this different geometry, the coarse-grained model continues to perform well. The discrepancies are primarily due to the small underestimation, shown in Figure 2, of the solvation free energy of small spheres. Figure 3 also compares the solvation free energies of plates with increasing attractions to the corresponding results from explicit-water simulations. Aside from the small artifacts already present in the ideal solute case, the contribution of the attractions to solvation free energies calculated with the coarse grained model is nearly quantitative.

B. Fluctuations

A more detailed probe of solvent behavior than solvation free energies is the probability $P_V(N)$ of finding N waters in a given volume V. The solvation free energy G of an ideal, volume-excluding hydrophobe is simply[33] $\beta G = -\ln P_V(0)$, and we can glean information about hydrophobicity and dewetting from the behavior at non-zero N.

In the present model, we estimate $P_V(N)$ by a two-step procedure. For any given solvent configuration $\{n_i\}$, the small length-scale fluctuations of $\delta\rho(\mathbf{r})$ give rise to a Gaussian distribution in the numbers of waters, so that

$$P_V(N|\{n_i\}) \propto \exp\big[-(N - \langle N\rangle_V)^2/2\sigma_V\big], \quad (16)$$

where,

$$\langle N\rangle_V = \sum_i n_i \Big[\rho_\ell V_i - \sum_j \chi_{ij}(V,v)n_j\langle N\rangle_v/\sigma_v \\ - \sum_j \chi_{ij}(V,\bar{v})n_j\beta(u_j + \phi_j)\Big], \quad (17)$$

and,

$$\sigma_V = \sum_{ij} n_i \chi_{ij}(V,V)n_j. \quad (18)$$

Here, V_i is the overlap of the probe volume with cell i. Notice the use of the probe volume V in the χ_{ij} matrices. Formally, we then thermally average the above result over all possible solvent configurations to obtain

$$P_V(N) \propto \sum_{\{n_i\}} P_V(N|\{n_i\})\exp(-\beta H_{\text{eff}}[\{n_i\}]).$$

In practice, we estimate this sum by sampling a lattice variable n that closely correlates with N, given by

$$n = \sum_{i \in V} n_i.$$

We divide the range of possible values of n into small overlapping windows, and sample relevant configurations at every value of n using Wang-Landau sampling[67] along n, together with replica exchange,[68] to obtain good sampling and avoid kinetic traps. We then used the multistate Bennet acceptance ratio estimator[69] (MBAR) to reconstruct from these runs the probability distribution $P(n)$. During the umbrella sampling runs, lattice configurations with equal n are observed in proportion to their Boltzmann weight. Using the notation $\{n_i\} \in n$ to denote all observed lattice gas configurations with a particular value of n, we finally obtain

$$P_V(N) = \sum_n P(n) \sum_{\{n_i\}\in n} P_V(N|\{n_i\}).$$

To estimate the statistical errors in our procedure, we calculate $P_V(N)$ in five independent Monte Carlo runs, and estimate the standard error in the mean of $\ln P_V(N)$.
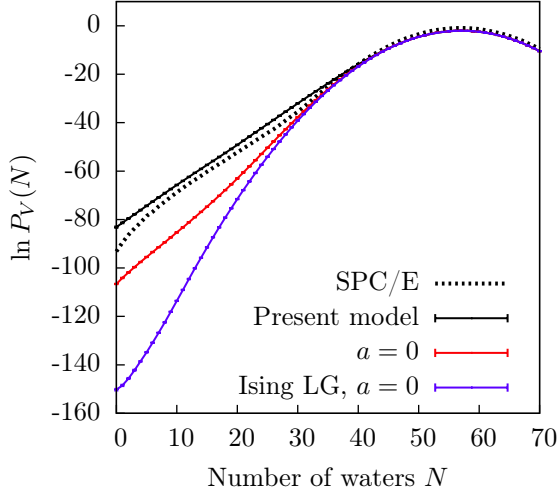
FIG. 4. Water number distribution in a $12 \times 12 \times 12\,\text{Å}^3$, as obtained using explicit SPC/E water simulations,[32] the present model, the present model without the unbalancing potential ($a = 0$), and a model with an Ising Lattice Gas and no unbalancing potential.
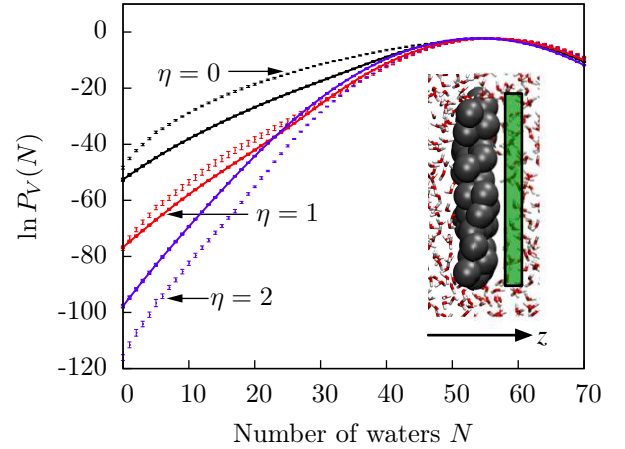

FIG. 5. Water number distributions in a probe volume of size $24 \times 24 \times 3\,\text{Å}^3$ immediately adjacent to a model plate solute (inset) of varying attractive strength η, in the coarse-grained model (solid lines) and in explicit SPC/E water (points). Defining $z = 0$ to be the plane passing through the plate center, points in the probe volume (green) satisfy $5\,\text{Å} < z < 8\,\text{Å}$, so that a water molecule touching the plate is located at the edge of the probe volume.[32]

For comparison, we also calculate these distributions in SPC/E water using LAMMPS[70] as described previously,[32] paying careful attention to good sampling around free energy barriers. Errors were estimated with MBAR.

In the absence of a solute, $P_V(N)$ is sensitive only to the interfacial energetics of the lattice gas. Figure 4 compares the $P_V(N)$ curve obtained using the present model for a $12 \times 12 \times 12\,\text{Å}^3$ volume with results that we have previously obtained from simulation of SPC/E water,[32] and with (a) a version of the coarse-grained model that lacks an unbalancing potential (a is set to zero), and (b) a version that additionally uses the naive Ising lattice gas for estimating interfacial energetics in $n(\mathbf{r})$. Our present model captures the observed deviations from Gaussian behavior better than these simpler models, which reflects its higher accuracy in estimating interfacial energetics and microscopic curvature effects.

We have also previously examined how hydrophobic solutes affect water number fluctuations in nearby probe volumes.[32] To evaluate the performance of our model in that scenario, we use the model hydrophobic plate solute described in Ref. 32. The plate is made up of oily particles with the same number density as water, whose centers lie inside a $24 \times 24 \times 3\,\text{Å}^3$ volume[71]. Taking into account the van der Waals radii of the oily particles, the plate has approximate dimensions $28 \times 28 \times 7\,\text{Å}^3$. We model this solute in the same way as the hexagonal plates described above. As before, we explore the role of attractive interactions by varying the attraction strength parameter η.

Figure 5 shows the water number distribution in a $24 \times 24 \times 3\,\text{Å}^3$ probe volume adjacent to the plate. With no solute-solvent attractive interactions, the probability computed from the lattice model has a clear fat tail towards lower numbers of waters in the probe volume. This fat tail is the hallmark of a soft vapor-liquid interface, in this case a soft interface next to the hydrophobic solute.[72–75] At higher attractive interactions, this fat tail is correspondingly depressed, but not entirely suppressed. Accordingly, in Ref. 32, the fat tail is only fully suppressed when η exceeds 3.0.

Figure 5 also evidences some of the limitations of the present model. The probe volume being less than one lattice cell thick, large lattice artifacts are inevitable. Moreover, since $P_V(N)$ distributions are much more detailed probes of solvent structure than solvation free energies, we expect more room for disagreement with simulation. Nevertheless, we emphasize that, by construction, no implicit solvation models can capture the above effects on solvent structure, which underlie the pathways of hydrophobic assembly. Other coarse-grained solvation models (for example, see Ref. 76), on the other hand, *can* probe rare solvent fluctuations, and it would be useful to evaluate their accuracy in this respect as compared to explicit-water models and the present lattice model.

C. Confinement

To examine confinement in detail, we place two of the model hydrophobic plates at a distance d from each other, as shown in Figure 6, and calculate the water number distribution in a $24 \times 24 \times (d - 3)\,\text{Å}$ probe volume between them as a function of interplate separation d and
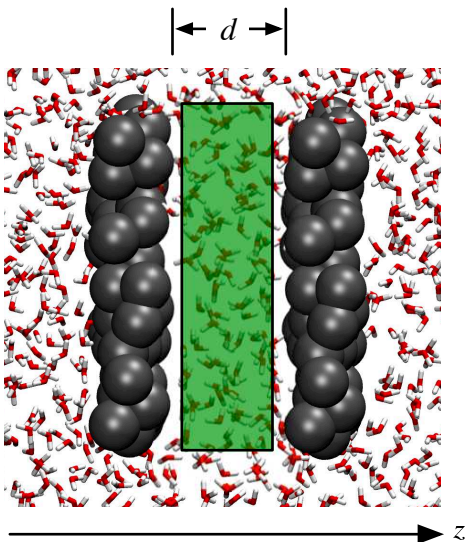
FIG. 6. Setup for examining water fluctuations under confinement (here, $d = 8\,\text{Å}$). The model hydrophobic plates[32] (grey particles) are placed $d\,\text{Å}$ apart: taking into account the van der Waals radii of about $2\,\text{Å}$ of the plates' oily particles and the $3\,\text{Å}$ thickness of each plate, the center of the first plate is placed at $z = 0$, the center of the second plate is placed at $z = d + 7\,\text{Å}$. The van der Waals radius of water (red and white sticks) being about $1.5\,\text{Å}$, the $24 \times 24 \times (d-3)\,\text{Å}^3$ probe volume (green) extends from $z = 5\,\text{Å}$ to $z = d + 2\,\text{Å}$. The plates are not perfectly flat, so some waters fit between the plates and the probe volume.
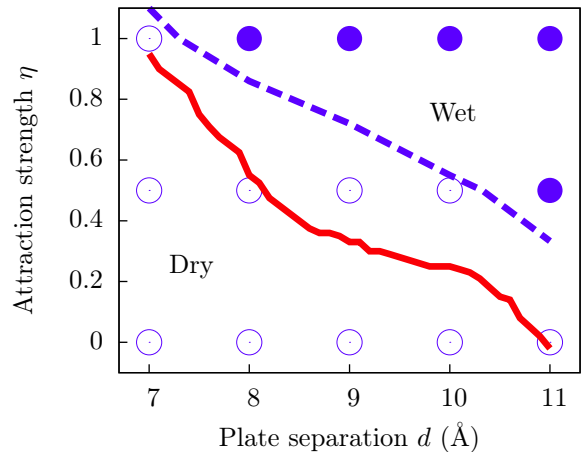

FIG. 7. Phase diagram for the interplate region of the system depicted in Figure 6. For the explicit SPC/E water simulations (blue), each symbol corresponds to an individual $P_V(N)$ distribution that we have calculated (filled: wet state stable; open: dry state stable). The phase boundary (blue dashes) is estimated from a linear interpolation of the relative stability of the wet and dry states. The relative stability is determined from the relative depths of the basins in $-\ln P_V(N)$ The phase boundary for the present model (red solid line) was estimated from a dense sampling of $P_V(N)$ distributions, and is accurate to $\pm 0.1\,\text{Å}$ in d and ± 0.1 in η.

attraction strength η. Figure 7 summarizes the results in the form of a phase diagram. At small separations and low attractive strengths, the dry state (low N) is most stable, whereas high attractive strengths and large separations stabilize the wet state (high N). Generically, the hydrophobic association of two such plates proceeds through a dewetting transition in the inter-plate volume.[22–24,26]

The general, though not quantitative, agreement between the coarse-grained model and the SPC/E data is very encouraging: bistability is observed in the $P_V(N)$ distributions in both cases, with the barriers at the nearly equal values of N, and with barrier heights that track the SPC/E barrier heights. The phase boundary in Figure 7 closely tracks the phase boundary observed in explicit water, with a shift of less than $2\,\text{Å}$ for all η. Moreover, as shown in Figure 8, once the general shift in the phase boundaries is accounted for, the $P_V(N)$ distributions for systems near that boundary obtained by the coarse-grained model and the SPC/E simulations agree reasonably well. Hence, the present model is better suited than implicit solvation models for studies of nanoscale self-assembly or protein-protein interactions driven by the hydrophobic effect. A recently developed coarse-grained model of water (mW water) has been used to extensively probe these rare fluctuations, and their predictions also display the characteristic bistability of dewetting transi-

tions that we observe.[36,77]

IV. DISCUSSION

We have presented a coarse-grained model of solvation thermodynamics that correctly reproduces the length-scale dependence of solvation free energies, and, moreover, correctly captures the behavior of the slow and rare solvent fluctuations that are pivotal in pathways to hydrophobic assembly. Our model is applicable to generic solute shapes, and addresses the effects of solute-solvent attractive interactions.

While our model successfully describes various aspects of the hydrophobic effect, several technical challenges must be addressed before it can be applied in biological settings. Most notably, electrostatic forces are missing from our model. As a first approximation, the GB treatment may well be sufficiently accurate, as long as the low-permittivity cavity includes both the solute's excluded volume and the regions where $n(\mathbf{r})$ is zero. It may also be possible to implement electrostatics in terms of a dipole density field coupled to the water density field. The statistics of the dipole field are known to be Gaussian[78,79] so that their contribution to $H_{\text{eff}}[\{n_i\}]$ may be computed analytically.

A second notable technical hurdle is to find efficient algorithms for calculating the gradient of $H_{\text{eff}}[\{n_i\}]$ with respect to the position of the solute's atomic centers, nec-
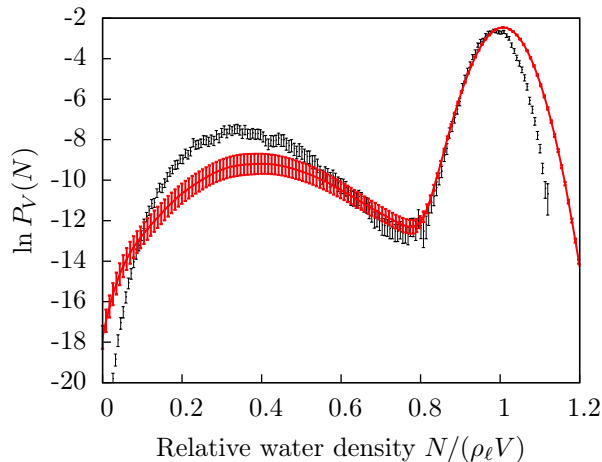
FIG. 8. Water density distribution of confined water $1\,\text{Å}$ from coexistence. These distributions are for the system depicted in Figure 6 when $\eta = 0.5$. Coexistence lines are shown in Figure 7. The explicit water simulation data (black) corresponds to $d = 11\,\text{Å}$, while the coarse-grained model (red) results correspond to $d = 9\,\text{Å}$. The remaining $P_V(N)$ distributions are included in the Supplementary Data[71].

essary for implementing realistic solute dynamics, such as Brownian dynamics. In the context of solvent lattice models, the problem is tractable for spherical solutes with limited overlap,[14,45] but the implementation of a solution for generic solutes is more challenging.

Finally, as with implicit solvation models, our own model does not attempt to capture solvent *dynamics*. For thermodynamically-driven processes, almost any reasonable dynamics may suffice when estimating the kinetic prefactor of rate constants of interest. Indeed, in a previous lattice model,[14] the solvent dynamics is approximated by Glauber dynamics, the solute's by Langevin dynamics, and the relative rates at which the two dynamics are advanced are calibrated through physically reasonable arguments. However, it is known, as evidenced in the form of the Oseen tensor, that hydrodynamic interactions can be long-ranged[80] and can influence timescales of molecular processes by one or more orders of magnitude.[81] This observation may prove important in nanoscale assembly processes that are kinetically driven, rather than thermodynamically driven.[82] Approaches to implementing coarse-grained dynamics in a lattice setting include multiparticle collision dynamics,[83] fluctuating hydrodynamics[84] and lattice Boltzmann methods,[85] among others. We leave all dynamical considerations to future work.

Appendix A: Derivation of the Model

1. Continuum formulation

In this appendix, we derive Equation (11) starting from the microscopic ideas of LCW theory embodied in Equation (2). The forms of $H_{\text{small}}[\delta\rho(\mathbf{r}); n(\mathbf{r})]$ and $H_{\text{large}}[n(\mathbf{r})]$ are given in Equations (3) and (9), and are discussed in the main text. Here, we begin by discussing the details of the $H_{\text{int}}[n(\mathbf{r}), \delta\rho(\mathbf{r})]$ term. Next, we integrate out the field $\delta\rho(\mathbf{r})$ to obtain the effective Hamiltonian $H_{\text{eff}}[n(\mathbf{r})]$. In the following section, we discretize it.

Whenever $n(\mathbf{r})$ is non-uniform, solvent molecules experience an effective attraction towards denser regions, or equivalently, an effective repulsion from less dense regions. As argued by Weeks and coworkers,[12,13,46] this effect can be modeled as a coupling, $H_{\text{int}}[n(\mathbf{r}), \delta\rho(\mathbf{r})]$, between an external *unbalancing* potential, $\phi(\mathbf{r})$, and solvent density. In the absence of a solute, the energetics of this effect is completely contained in $H_{\text{large}}[n(\mathbf{r})]$, but the presence of a solute gives rise to important corrections. Formally, the coupling is given by

$$H_{\text{int}}[n(\mathbf{r}), \delta\rho(\mathbf{r})] = \int_{\mathbf{r}} \phi(\mathbf{r})\delta\rho(\mathbf{r}) + H_{\text{norm}}[n(\mathbf{r})], \quad \text{(A1)}$$

where

$$\phi(\mathbf{r}) = -2a\rho_\ell[\overline{n(\mathbf{r})} - 1]. \quad \text{(A2)}$$

Here, a determines the strength of the potential, and the overbar operator smears $n(\mathbf{r})$ over the effective range of solvent-solvent attractive interactions. The potential is shifted so that it is zero for the uniform liquid. The term $H_{\text{norm}}[n(\mathbf{r})]$ is chosen so that, in the absence of a solute, $H_{\text{eff}}[n(\mathbf{r})]$ is identical to $H_{\text{large}}[n(\mathbf{r})]$.

We now integrate out the field $\delta\rho(\mathbf{r})$ to obtain $H_{\text{eff}}[n(\mathbf{r})]$. For notational simplicity, we suppress the dependence of $\chi(\mathbf{r}, \mathbf{r}')$ on $n(\mathbf{r})$ manifest in Equation (4). The total density $\rho_\ell n(\mathbf{r}) + \delta\rho(\mathbf{r})$ is constrained to be zero for all points $\mathbf{r}$ in v, so the effective Hamiltonian is given by

$$\exp\{-\beta H_{\text{eff}}[n(\mathbf{r})]\} = \int \mathcal{D}\delta\rho(\mathbf{r})$$
$$\exp\{-\beta H[n(\mathbf{r}), \delta\rho(\mathbf{r})]\} \prod_{\mathbf{r}\in v} \delta(\rho_\ell n(\mathbf{r}) + \delta\rho(\mathbf{r})). \quad \text{(A3)}$$

A long but straightforward calculation[42] yields

$$H_{\text{eff}}[n(\mathbf{r})] = H_{\text{large}}[n(\mathbf{r})] + k_{\text{B}}T \ln \sqrt{\det 2\pi\chi_v} - \int_{\mathbf{r}\in v} \phi(\mathbf{r})\rho_\ell n(\mathbf{r})$$

$$+ \frac{k_{\text{B}}T}{2} \int_{\mathbf{r}\in v} \int_{\mathbf{r}'\in v} \left[\rho_\ell n(\mathbf{r}) - \int_{\mathbf{r}''\in\bar{v}} \chi(\mathbf{r},\mathbf{r}'')\beta\phi(\mathbf{r}'')\right] \chi_v^{-1}(\mathbf{r},\mathbf{r}') \left[\rho_\ell n(\mathbf{r}') - \int_{\mathbf{r}'''\in\bar{v}} \chi(\mathbf{r}',\mathbf{r}''')\beta\phi(\mathbf{r}''')\right]$$

$$- \frac{k_{\text{B}}T}{2} \int_{\mathbf{r}\in\bar{v}} \int_{\mathbf{r}'\in\bar{v}} \beta\phi(\mathbf{r})\chi(\mathbf{r},\mathbf{r}')\beta\phi(\mathbf{r}') + H_{\text{norm}}[n(\mathbf{r})]. \quad \text{(A4)}$$

Here, $\chi_v(\mathbf{r},\mathbf{r}')$ is the restriction of $\chi(\mathbf{r},\mathbf{r}')$ to the volume v. As such, $\chi_v^{-1}(\mathbf{r},\mathbf{r}')$ satisfies

$$\int_{\mathbf{r}'\in v} \chi_v^{-1}(\mathbf{r},\mathbf{r}')\chi(\mathbf{r}',\mathbf{r}'') = \delta(\mathbf{r}-\mathbf{r}''), \qquad \mathbf{r},\mathbf{r}'' \in v. \quad \text{(A5)}$$

To make $H_{\text{eff}}[n(\mathbf{r})]$ equal to $H_{\text{large}}[n(\mathbf{r})]$ in the absence of a solute,

$$H_{\text{norm}}[n(\mathbf{r})] = \frac{k_{\text{B}}T}{2} \int_{\mathbf{r}} \int_{\mathbf{r}'} \beta\phi(\mathbf{r})\chi(\mathbf{r},\mathbf{r}')\beta\phi(\mathbf{r}'). \quad \text{(A6)}$$

It is useful to recast Equation (A4) into a form where the physical significance of each term is manifest. To do so, we first note how the constraint of zero solvent density inside v modifies the solvent density and its fluctuation spectrum outside of v. As described in Ref. 42, the average of $\delta\rho(\mathbf{r})\delta\rho(\mathbf{r}')$ in the presence of the constraint, denoted by $\chi^{(\text{m})}(\mathbf{r},\mathbf{r}')$, is given by

$$\chi^{(\text{m})}(\mathbf{r},\mathbf{r}') = \chi(\mathbf{r},\mathbf{r}')$$
$$- \int_{\mathbf{r}''\in v} \int_{\mathbf{r}'''\in v} \chi(\mathbf{r},\mathbf{r}'')\chi_v^{-1}(\mathbf{r}'',\mathbf{r}''')\chi(\mathbf{r}''',\mathbf{r}'). \quad \text{(A7)}$$

From Equation (A5), it follows that $\chi^{(\text{m})}(\mathbf{r},\mathbf{r}')$ is zero whenever $\mathbf{r}$ or $\mathbf{r}'$ are in v, as required by the solvent exclusion constraint. To describe the constraint's effect on the average density, we introduce an auxiliary field $c(\mathbf{r})$ that satisfies

$$\int_{\mathbf{r}'\in v} \chi(\mathbf{r},\mathbf{r}')c(\mathbf{r}') = \rho_\ell n(\mathbf{r}), \qquad \mathbf{r}\in v, \quad \text{(A8a)}$$

$$c(\mathbf{r}) = 0, \qquad \mathbf{r}\in\bar{v}. \quad \text{(A8b)}$$

In terms of $c(\mathbf{r})$ and $\chi^{(\text{m})}$, the average density in the presence of the solute is given by

$$\langle\rho(\mathbf{r})\rangle = \rho_\ell n(\mathbf{r})$$
$$- \int_{\mathbf{r}'\in v} \chi(\mathbf{r},\mathbf{r}')c(\mathbf{r}') - \int_{\mathbf{r}'\in\bar{v}} \chi^{(\text{m})}(\mathbf{r},\mathbf{r}')\beta\phi(\mathbf{r}'). \quad \text{(A9)}$$

Equation (A4) can now be written much more simply

as follows.

$$H_{\text{eff}}[n(\mathbf{r})] = H_{\text{large}}[n(\mathbf{r})] - \int_{\mathbf{r}\in v} \phi(\mathbf{r})\rho_\ell n(\mathbf{r})$$

$$+ k_{\text{B}}T \ln \sqrt{\det 2\pi\chi_v} + \frac{k_{\text{B}}T}{2} \int_{\mathbf{r}\in v} \rho_\ell n(\mathbf{r})c(\mathbf{r})$$

$$- \int_{\mathbf{r}\in\bar{v}} \int_{\mathbf{r}'\in v} \phi(\mathbf{r})\chi(\mathbf{r},\mathbf{r}')c(\mathbf{r}')$$

$$+ \frac{k_{\text{B}}T}{2} \int_{\mathbf{r}} \int_{\mathbf{r}'} \beta\phi(\mathbf{r})(\chi - \chi^{(\text{m})})(\mathbf{r},\mathbf{r}')\beta\phi(\mathbf{r}'). \quad \text{(A10)}$$

For the geometries we considered, the sum of the last two terms of this equation is, on average, opposite in sign but nearly proportional to the much simpler remaining term involving $\phi(\mathbf{r})$ (see Section D). Physically, these three terms capture the energetic bonus of driving $\delta\rho(\mathbf{r})$ to 0 inside v where ϕ is positive, the energetic cost of the consequent density enhancement just outside of v, and the small difference between (a) the entropic cost associated with ϕ modifying the solvent density in the presence of a solute and (b) that same cost in the absence of a solute. In typical configurations, the three terms are roughly proportional to the subvolume of v where $n(\mathbf{r}) = 1$, and capture how solvation free energies are modified by the microscopic curvature of v. We have found it accurate to model the effect of these three terms using *only* the second term of Equation (A10), whose strength is then renormalized by a factor K. The resulting approximation for $H_{\text{int}}[n(\mathbf{r})]$ is

$$H_{\text{int}}[n(\mathbf{r})] \approx -K \int_{r\in v} \phi(\mathbf{r})\rho_\ell n(\mathbf{r}). \quad \text{(A11)}$$

Finally, we introduce an important simplification in $H_{\text{small}}[n(\mathbf{r})]$. Instead of solving Equation (A8a) to obtain the value of the field $c(\mathbf{r})$ in v, we replace $c(\mathbf{r})$ there by its average value, c_1, and obtain the much simpler relation

$$c_1 = \langle N\rangle_v / \sigma_v, \quad \text{(A12)}$$

where

$$\langle N\rangle_v = \int_{\mathbf{r}\in v} \rho_\ell n(\mathbf{r}), \quad \text{(A13)}$$

$$\sigma_v = \int_{\mathbf{r}\in v} \int_{\mathbf{r}'\in v} \chi(\mathbf{r},\mathbf{r}'). \quad \text{(A14)}$$

Equivalently, in Equation (A3) we enforce the single constraint that $\int_{\mathbf{r} \in v} \rho_\ell n(\mathbf{r}) + \delta\rho(\mathbf{r})$ be zero, instead of enforcing the multitude of constraints that $\rho_\ell n(\mathbf{r}) + \delta\rho(\mathbf{r})$ be zero at every point $\mathbf{r}$ in v. We have verified that this approximation, dubbed the "one-basis set approximation" in previous works,[13,52] does not appreciably change the solvation free energies and $P_V(N)$ distributions that we have obtained. Crucially, this approximation replaces the large (though sparse) linear system of Equation (A8a) with the trivial relation of Equation (A12), and is therefore very advantageous computationally. With it, the term $H_{\text{small}}[n(\mathbf{r})]$ is given by

$$H_{\text{small}}[n(\mathbf{r})] = k_B T[\langle N \rangle_v^2 / 2\sigma_v + C/2], \qquad \text{(A15)}$$

The normalization constant C is defined by Equation (11e). When the value of $\langle N \rangle_v$ becomes small, the integral defining σ_v is dominated by the δ-function in Equation (5) and takes the value $\sigma_v \approx \langle N \rangle_v$. The value $\ln(2\pi\sigma_v)$ of C that is applicable for larger $\langle N \rangle_v$ thus tends unphysically to negative infinity as $\langle N \rangle_v$ tends to zero. This deficiency arises from a breakdown of Gaussian statistics for solvent number fluctuations in sub-Angstrom volumes. Since solvent molecules are discrete entities, these statistics are instead Poissonian. A small cavity v can contain either one solvent molecule, with probability $\langle N \rangle_v$, or no solvent molecules, with probability $1 - \langle N \rangle_v$. The free-energy cost of evacuating that cavity is thus $-k_B T \ln(1 - \langle N \rangle_v) \approx \langle N \rangle_v k_B T$. The definition of C given in Equation (11e) is a simple, continuous way of capturing this difference in fluctuation statistics at tiny length-scales. The crossover occurs at $\langle N \rangle_v \approx (2\pi - 2)^{-1} \approx 0.23$.

2. Lattice formulation

Using Equation (6), we express $H_{\text{eff}}[n(\mathbf{r})]$ and its component terms in terms of the lattice variables n_i, so that

$$H_{\text{eff}}[\{n_i\}] = H_{\text{large}}[\{n_i\}] + H_{\text{int}}[\{n_i\}] + H_{\text{small}}[\{n_i\}]. \qquad \text{(A16)}$$

The integrals that define each term are then approximated through lattice sums, with continuous fields replaced by either their average values or their integrals over each cell.

Equation (A15) for $H_{\text{small}}[\delta\rho(\mathbf{r}); n(\mathbf{r})]$ is the easiest to tackle. We begin by discretizing Equation (4), which defines $\chi(\mathbf{r}, \mathbf{r}')$, when the domains of integration for $\mathbf{r}$ and $\mathbf{r}'$ are V and V', respectively. In terms of the matrix $\chi_{ij}(V, V')$ defined by Equation (8), our prescription yields

$$\chi(\mathbf{r}, \mathbf{r}') \to n_i \chi_{ij}(V, V') n_j, \qquad \mathbf{r} \in V, \mathbf{r}' \in V'.$$

Equation (11d) for σ_v then follows immediately from Equation (A14). Equation (11c) for $\langle N \rangle_v$ reasonably approximates the integral in Equation (A13).

To discretize Equation (A11) for $H_{\text{int}}[n(\mathbf{r})]$, we need to choose a concrete implementation of the overbar operation that is used to define $\phi(\mathbf{r})$. Following Ref. 13, we approximate it as a weighted average involving the cell and its nearest neighbors[86], given by

$$\overline{n(\mathbf{r})} \to \left[\frac{1}{2} n_i + \frac{1}{12} \sum_{j \, (\text{nn}i)} n_j \right].$$

The average, ϕ_i, of $\phi(\mathbf{r})$ over cell i follows immediately from Equation (A2), and is given by Equation (11b). Following our prescription, Equation (A11) is then reasonably discretized as the lattice sum

$$H_{\text{int}}[\{n_i\}] \approx K \sum_i \phi_i(-\rho_\ell n_i v_i).$$

Discretizing $H_{\text{large}}[n(\mathbf{r})]$ correctly is a surprisingly subtle challenge. Previously,[13,14,45] it has been approximated it by an Ising Hamiltonian with nearest-neighbor coupling

$$H_{\text{large}}[\{n_i\}] \xrightarrow{?} \gamma\lambda^2 \sum_{\langle ij \rangle} (n_i - n_j)^2 - \mu\rho_\ell\lambda^3 \sum_i n_i.$$

Unfortunately, the use of this Hamiltonian results in serious artifacts. Consider, for instance, the energetics of a convex vapor bubble embedded in the liquid, as represented by the field $\{n_i\}$. Many configurations of the field that are physically distinct have nonetheless equal projections onto the xy-, yz- and xz-planes, so they will be given equal statistical weight by the Hamiltonian. Hence, the use of this Hamiltonian results in an unphysical excess of entropy, as shown in detail in Section E. Moreover, the energetic cost of common configurations of the field $\{n_i\}$ is substantially overestimated. The Ising Hamiltonian assigns a large vapor bubble of radius R an interfacial energy of about $6\pi\gamma R^2$, not $4\pi\gamma R^2$. Whereas using a renormalized γ can alleviate this latter problem,[27] the problem of excess entropy is more fundamental.

Motivated by the above deficiencies of the Ising Hamiltonian, we have instead chosen to evaluate the Landau-Ginzburg integral in Equation (9) numerically. To proceed, we need to construct the basis function $\Psi(\mathbf{r})$ used in Equation (6). Our choice, depicted in Figure 9 for water, approximates the usual van der Waals construction[87] at a local level. We first construct a 1D basis function $\psi(x)$ satisfying

$$w'(\psi(x), 0) - m\psi''(x) = 0, \qquad \text{(A17)}$$

with boundary conditions $\psi(0) = 1$ and $\psi(\lambda) = 0$. We then extend the range of $\psi(x)$ and symmetrize it so that

$$\psi(x > \lambda) = 0, \qquad \text{(A18)}$$
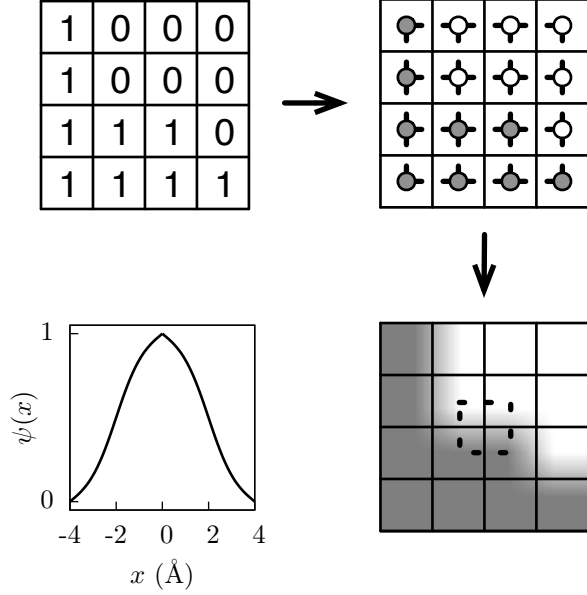
and

$$\psi(x < 0) = \psi(-x). \qquad \text{(A19)}$$

FIG. 9. Constructing $n(\mathbf{r})$ from $\{n_i\}$. The binary field specifies whether the density at the center of each lattice cell should be that of the liquid or that of the vapor. Between cell centers, the density is interpolated using the basis function $\psi(x)$ (whose form for water is shown in the lower left panel). The dashed lines delineate the domain of integration of the local free energy h_i given by Equation (10).

Finally, the three-dimensional basis function $\Psi(\mathbf{r})$ is constructed from the one-dimensional profiles $\psi(x)$ to give

$$\Psi(x, y, z) = \psi(x)\psi(y)\psi(z).$$

The field $n(\mathbf{r})$ constructed from Equation (6) using this basis function has many useful properties: the value of $n(\mathbf{r})$ at the center of each cell i corresponds to the state encoded in n_i; the density interpolates smoothly between adjacent cells; and the density profile of a configuration representing an axis-aligned wall, where all n_i's are 1 on one side of a plane and 0 on the other, nearly reproduces the interface profile given by the van der Waals construction.

For water, we use the function $w(n, \mu)$ given in Equation (14). This choice results in both sides of Equation (A17) being proportional to m, so the function $\psi(x)$ is independent of m. In the free van der Waals theory, where the boundary conditions on Equation (A17) are $\psi(-\infty) = 1$ and $\psi(+\infty) = 0$, the density profile $\psi_0(z)$ that results is

$$\psi_0(z) = [1 + \tanh(z/d)]/2,$$

which accurately describes the average density profile of an SPC/E water slab at ambient conditions. The thickness parameter d can thus be determined from simulation. A complication due to capillary waves is that d grows logarithmically with simulation box size,[72,88] so different authors quote different values of d: $1.27\,\text{Å}$ for a $19 \times 19\,\text{Å}^2$ interface in Ref. 52 and $1.54\,\text{Å}$ for a $30 \times 30\,\text{Å}^2$ interface in Ref. 89. We choose the smaller value because the instantaneous configuration of $n(\mathbf{r})$ should be blurred only by small-scale fluctuations, not by large-scale capillary waves, which correspond instead to different conformations of $n(\mathbf{r})$. The profile shown in Figure 9 corresponds to the solution of Equation (A17) when the more restrictive boundary conditions described above are imposed, with $\lambda = 4\,\text{Å}$ and $d = 1.27\,\text{Å}$.

With concrete choices of $\Psi(\mathbf{r})$, $w(n, 0)$, m and λ, the integrals h_i defined by Equation (10) can be evaluated. We discuss the choice of m below. As outlined in the main text, the value of h_i depends only on the values of n_j for the 8 cells j that share one of the corners of cell i. Out of the 256 possible configurations of $\{n_j\}$, only 14 are unique when one accounts for reflection, rotation and inversion symmetry. Thus, only 14 distinct integrals need to be evaluated numerically. This decomposition bears a strong resemblance to the marching cubes algorithm[90] that reconstructs interfaces in volumetric data, and is widely used in computerized tomography.

In principle, the value of m is related to the surface tension by the relation[87]

$$\gamma = \int_0^\lambda \Big[w(\psi(x), 0) + m\psi'(x)^2/2 \Big]\,\mathrm{d}x. \qquad (A20)$$

On a lattice, as exemplified above by the Ising Hamiltonian, this choice results in perfect interfacial energies for flat axis-aligned interfaces at the expense of more common curved interfaces. Thus, we instead choose m self-consistently such that $\psi(x)$ satisfies Equation (A17) and the calculated interfacial energy of some reference geometry of surface area A is γA. Equation (A20) corresponds to a cubic reference geometry. Since curved surfaces are far more common than flat one in realistic solutes, we instead use large spheres as our reference geometry.

For the specific form of $w(n)$ that we use for water, h_i is proportional to m and $\psi(x)$ is itself independent of m. The above self-consistent procedure can hence be implemented quite simply. We first calculate the h_i quantities up to a factor of m, and then pick m to obtain the correct interfacial energies. The resulting values of h_i are given in Table I.

3. Incorporating solute-solvent interactions

A generic solute interacts with a solvent molecule through a potential $u(\mathbf{r})$. This interaction is reflected in the microscopic Hamiltonian of Equation (2) as an additional term $H_u[n(\mathbf{r}), \delta\rho(\mathbf{r})]$ given by

$$H_u[n(\mathbf{r}), \delta\rho(\mathbf{r})] = \int_\mathbf{r} u(\mathbf{r})[\rho_\ell n(\mathbf{r}) + \delta\rho(\mathbf{r})].$$

Upon integrating out the density fluctuations, an additional term $H_u[n(\mathbf{r})]$ appears in $H_{\mathrm{eff}}[n(\mathbf{r})]$. Physically,

TABLE I. Relative interfacial free energy h_i for each distinct neighboring cell configuration (diagrams after Ref. 90). Highlighted corners denote cells j with $n_j = 1$, whereas the others refer to cells with $n_j = 0$; cell i is the lower-left corner in the back. To aid the eye, a schematic of the implied liquid-vapor interface of each configuration is shown in orange. The values of h_i are inversion-symmetric: interchanging highlighted and unhighlighted corners yields the same interface and interfacial energy. Also shown are the values of h_i that would reproduce the energetics of the standard Ising lattice gas, namely $\gamma\lambda^2 \sum_{\langle ij \rangle}(n_i - n_j)^2$.

Local $\{n_j\}$ configuration							
h_i (Present model)	0.000	0.387	0.676	0.725	0.754	0.851	0.965
h_i (Ising model)	0.000	0.750	1.000	1.500	1.500	1.250	1.750
Local $\{n_j\}$ configuration							
h_i (Present model)	0.983	0.857	0.910	1.104	0.965	1.040	1.134
h_i (Ising model)	2.250	1.000	1.500	2.000	1.500	2.000	3.000

the total solvent density responds linearly to the external field $u(\mathbf{r})$ according to the density fluctuation spectrum is given by $\chi^{(\mathrm{m})}(\mathbf{r}, \mathbf{r}')$, so that

$$\langle \rho(\mathbf{r}) \rangle = \rho_\ell n(\mathbf{r}) - \int_{\mathbf{r}'} \chi(\mathbf{r}, \mathbf{r}') c(\mathbf{r}')$$
$$- \int_{\mathbf{r}'} \chi^{(\mathrm{m})}(\mathbf{r}, \mathbf{r}') \beta[\phi(\mathbf{r}') + u(\mathbf{r}')]. \quad (A21)$$

The resulting free energy change $H_u[n(\mathbf{r})]$ arises from the direct interaction of the solute and the solvent, and from the entropic cost of modifying the mean solvent density around the solute. It is given by

$$H_u[n(\mathbf{r})] = \int_{\mathbf{r}} \mathrm{d}\mathbf{r} \, u(\mathbf{r}) \langle \rho(\mathbf{r}) \rangle$$
$$+ \frac{k_{\mathrm{B}}T}{2} \int_{\mathbf{r}} \int_{\mathbf{r}'} \beta u(\mathbf{r}) \chi^{(\mathrm{m})}(\mathbf{r}, \mathbf{r}') \beta u(\mathbf{r}'). \quad (A22)$$

Note that the integrands are zero whenever $\mathbf{r}$ or $\mathbf{r}'$ are inside the solute.

To implement the previous equation on a lattice, we have found it useful to approximate $\chi^{(\mathrm{m})}(\mathbf{r}, \mathbf{r}')$ by

$$\chi^{(\mathrm{m})}(\mathbf{r}, \mathbf{r}') \approx \begin{cases} \chi_0(\mathbf{r} - \mathbf{r}'), & \mathbf{r}, \mathbf{r}' \in \bar{v}, n(\mathbf{r}) = n(\mathbf{r}') = 1, \\ 0, & \text{otherwise.} \end{cases}$$
$$(A23)$$

We also use the one-basis set approximation, $c(\mathbf{r}) \approx c_1$, given in Equation (A12). Discretizing Equation (A22) as in the previous section then immediately yields Equation (13).

Appendix B: Estimating $\chi_{ij}(V, V')$

An essential ingredient of the model we present is the matrix $\chi_{ij}(V, V')$, given by the integral in Equation (8).

The terms involving the delta-functions of Equation (4) are trivial. Owing to the rapid oscillations in $g(r) - 1$, the remaining integrals are harder to estimate. We employ a two-step procedure to estimate these integrals efficiently. We begin by subdiving the $\lambda = 4\,\text{Å}$-resolution grid of cells into a much finer grid of resolution $\lambda_f = 1\,\text{Å}$. For clarity, below we explicitly distinguish between cells in the *coarse* grid, indexed by the letters i and j, and cells in the *fine* grid, indexed by the letters a and b. We evaluate the integrals of the non-delta-function portion of χ_0 on the fine grid without otherwise restricting the arguments to particular volumes V and V', and denote the result by χ_{ab}. Each fine cell is so small that the effect of a restriction on the integration domain can be estimated accurately with a simple interpolation formula. We then use these interpolated values in the fine grid to build up the elements of $\chi_{ij}(V, V')$ over the coarse grid.

To evaluate χ_{ab}, we use the Narten-Levy data for the structure factor $S(k)$ of water.[54] Since the $S(k)$ is unavailable for wave-numbers k higher than $16\,\text{Å}^{-1}$, we blur the domains of integration over a range of about $2\pi/16\,\text{Å}$, which makes the values of the integrals practically insensitive to this missing data. Concretely, we introduce a basis function Φ, given by

$$\Phi(x, y, z) = \varphi(x)\varphi(y)\varphi(z),$$

with

$$\varphi(x) = \frac{1}{2}\left[\tanh\frac{x - \lambda_f/2}{\Delta} - \tanh\frac{x + \lambda_f/2}{\Delta}\right].$$

The function φ is unity around $x = 0$, and goes rapidly to zero as $|x| \gtrsim \lambda_f/2$, with Δ controlling the range of x over which this transition occurs. We have found a value of $0.1\,\text{Å}$ for Δ to be adequate. Using the notation $\mathbf{r}_a$ to denote the center of fine cell a, the value of χ_{ab} is given

by

$$\chi_{ab} = \rho_\ell^2 \int_{\mathbf{r}} \int_{\mathbf{r}'} \Phi(\mathbf{r} - \mathbf{r}_a)[g(|\mathbf{r} - \mathbf{r}'|) - 1]\Phi(\mathbf{r}' - \mathbf{r}_b). \quad \text{(B1)}$$

The integral is best evaluated in Fourier space, where the term in square brackets appears as the experimental $S(k)$ profile. We overcome the convergence problems of a rapidly oscillating integrand by using the Haselgrove-Conroy integration algorithm.[91,92] To properly account for $g(r)$ being exactly zero for $r \lesssim 2.35\,\text{Å}$, we further set χ_{ab} to exactly $-\rho_\ell^2$ if all points in a are within $r_c = 2.35\,\text{Å}$ from all points in b. To limit the range of χ_{ab}, we also set it to zero if all points in a are more than $10\,\text{Å}$ from all point in b. The values of χ_{ab} need only be calculated once at each state point of water, and we have spent considerable effort in compiling them at ambient conditions. Our results are included in the Supplementary Data[71].

For specific volumes V and V', we estimate the value of $\chi_{ij}(V, V')$ as a weighted average of the pertinent values of χ_{ab},

$$\chi_{ij}(V, V') \approx \rho_\ell(V \cap V') + \sum_{a \in i} \sum_{b \in j}(V_a/\lambda_f^3)\chi_{ab}(V_b'/\lambda_f^3), \quad \text{(B2)}$$

where $(V \cap V')$ is the volume of the overlap between V and V'. This interpolation formula for χ_{ij} is manifestly linear in its arguments, so that

$$\chi_{ij}(V, V') + \chi_{ij}(V, V'') = \chi_{ij}(V, V' \cup V''),$$

whenever V' and V'' do not overlap. Most importantly, the interpolation procedure is simple, convenient, and correct for the limiting cases of where all the values of V_a are either 0 or λ_f^3.

For comparison, we have also calculated values of χ_{ab} from an explicit SPC/E water simulation in GROMACS at temperature $T = 298\,\text{K}$ and pressure $p = 1\,\text{atm}$. The values are also included in the Supplementary Data[71]. For the quantities we have studied in the main text, using these values for χ_{ab} instead of those derived from the Narten-Levy data yields nearly identical results.

Appendix C: Fluctuation variance

The variance of the field $\delta\rho(\mathbf{r})$ given in Equation (4) is a simplification of the LCW interpolation formula,

$$\chi_{\text{LCW}}(\mathbf{r}, \mathbf{r}') = \rho_\ell n(\mathbf{r})\delta(\mathbf{r} - \mathbf{r}') + \rho_\ell^2 n(\mathbf{r})[g(|\mathbf{r} - \mathbf{r}'|) - 1]n(\mathbf{r}'),$$

to the case where $n(\mathbf{r})$ only takes the values 0 or 1. The discrepancies arising from using Equation (4) and more precise expressions for the variance are mostly quantitative and limited to the vicinity of liquid-vapor interfaces.[44]

One possible improvement to Equation (4) is given in Ref. 42:

$$\chi(\mathbf{r}, \mathbf{r}') = \chi_0(\mathbf{r}, \mathbf{r}') -$$
$$\int_{\mathbf{r}'' \in E} d\mathbf{r}'' \int_{\mathbf{r}''' \in E} d\mathbf{r}''' \chi_0(\mathbf{r}, \mathbf{r}'')\chi_E^{-1}(\mathbf{r}'', \mathbf{r}''')\chi_0(\mathbf{r}''', \mathbf{r}'), \quad \text{(C1)}$$

where E is the empty (i.e., gaseous) region of space where $n(\mathbf{r})$ is 0, and $\chi_E^{-1}(\mathbf{r}, \mathbf{r}')$ satisfies

$$\int_{\mathbf{r}'' \in E} \chi_E^{-1}(\mathbf{r}, \mathbf{r}'')\chi_0(\mathbf{r}'', \mathbf{r}') = \delta(\mathbf{r} - \mathbf{r}'), \quad \mathbf{r}, \mathbf{r}' \in E.$$

Equations (C1) and (4) are in qualitatively agreement: both are zero when $\mathbf{r}$ or $\mathbf{r}'$ are in the gaseous region, and both reduce to $\chi_0(\mathbf{r}, \mathbf{r}')$ well into the liquid phase. The differences are, as expected, concentrated near the boundaries of E. In this refined expression, the integrand oscillates significantly within a lattice cell, so a lattice approximation to Equation (C1) proves unreliable. Because using Equation (4) gives accurate results for all quantities we have examined, we regard the approximate Equation (4) to be acceptable, and we have not pursued algorithms by which Equation (C1) can be accurately evaluated.

Appendix D: How well is the effect of unbalanced forces captured by Equation (A11)?

Above, we replaced the three terms involving ϕ_i in Equation (A10) by the simpler expression given in (A11). We now justify this replacement.

Denote by $H_+[n(\mathbf{r})]$ the terms dropped from Equation (A10). They are

$$H_+[n(\mathbf{r})] = -\int_{\mathbf{r} \in \bar{v}} \int_{\mathbf{r}' \in v} \phi(\mathbf{r})\chi(\mathbf{r}, \mathbf{r}')c(\mathbf{r}')$$
$$+ \frac{k_B T}{2} \int_{\mathbf{r}} \int_{\mathbf{r}'} \beta\phi(\mathbf{r})(\chi - \chi^{(m)})(\mathbf{r}, \mathbf{r}')\beta\phi(\mathbf{r}'). \quad \text{(D1)}$$

Using the approximation for $\chi^{(m)}$ given in Equation (A23) and the one-basis set approximation of Equation (A12), we discretize these terms to obtain a lattice version of $H_+[n(\mathbf{r})]$,

$$H_+[\{n_i\}] = -\sum_{i,j} \phi_i n_i \chi_{ij}(\bar{v}, v)n_j\langle N\rangle_v/\sigma_v$$
$$+ k_B T \sum_{i,j} \beta\phi_i n_i[\chi_{ij}(v, v)/2 + \chi_{ij}(\bar{v}, v)]n_j\beta\phi_j.$$

Because of the double sums in the formula, calculating $H_+[\{n_i\}]$ is by far the most computationally-demanding part of calculating $H_{\text{eff}}[\{n_i\}]$. Since a single cell flip changes the value of ϕ_i in up to 7 cells, calculating incremental changes to $H_+[\{n_i\}]$ is also much more expensive than calculating incremental changes to $H_u[\{n_i\}]$ (Equation (13)), which has a similar structure.
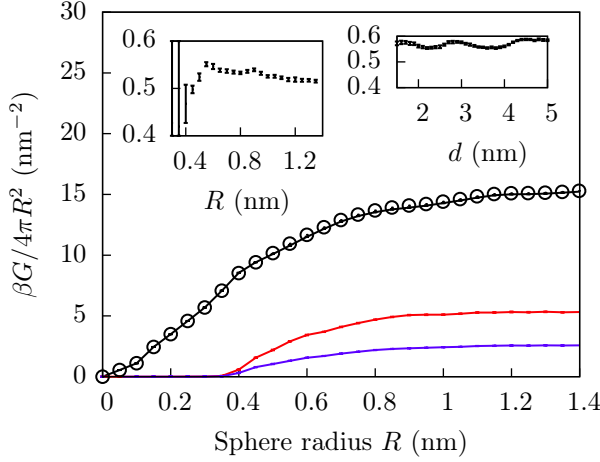
FIG. 10. Solvation free energies G of hard spheres as a function of sphere radius, where the term $H_+[\{n_i\}]$ (Equation (D1)) has been included and the renormalization constant K has been set to 1 (solid black), compared to the simpler model in Equation (11) (circles). The averages of $-\langle H_{\text{int}}[\{n_i\}]\rangle$ (red) and $\langle H_+[\{n_i\}]\rangle$ (black) are nearly proportional to each other. Left Inset: implied renormalization constant K, equal to $\langle H_{\text{int}}[\{n_i\}] + H_+[\{n_i\}]\rangle/\langle H_{\text{int}}[\{n_i\}]\rangle$. Note that both the numerator and denominator take on essentially zero value for $R \lesssim 0.4\,\text{nm}$. Right Inset: Implied value of K for hexagonal plate solute (Figure 3) with $\eta = 1.0$. The implied value of K is similar for different η.

Figure 10 presents the solvation free energies of hard spheres calculated when the $H_+[\{n_i\}]$ term is included and the renormalization constant K is set to 1. As can be seen, the term corresponding to $H_{\text{int}}[\{n_i\}]$ has a much larger absolute value, and in the region where their values are not negligible, the average values of $H_{\text{int}}[\{n_i\}]$ and $H_+[\{n_i\}]$ are, as claimed, essentially proportional. The renormalization procedure we implement thus seems justified, a conclusion borne out by the results in the text. For completeness, we have verified that the solvation free energies of the hexagonal plate solute (Figure 3) calculated when $H_+[\{n_i\}]$ is included and K is 1 are essentially identical to the ones calculated using Equation (11).

Appendix E: Comparison to the model of ten Wolde and Chandler

Above, we argued that the Ising Hamiltonian estimate for $H_{\text{large}}[n(\mathbf{r})]$ overestimates the interfacial energy of a sphere of radius R by a factor of $3/2$. However, the lattice version of LCW theory presented by ten Wolde and Chandler[14] uses precisely this Hamiltonian, yet the solvation free energy of spheres seems to tend to the correct value as R grows. Here we explain this apparent paradox.

Figure 11 shows the solvation free energies of spheres in the model of Ref. 14, and shows how they differ when the lattice cell size of $\lambda = 2.1\,\text{Å}$ is changed to $\lambda = 2.3\,\text{Å}$. As
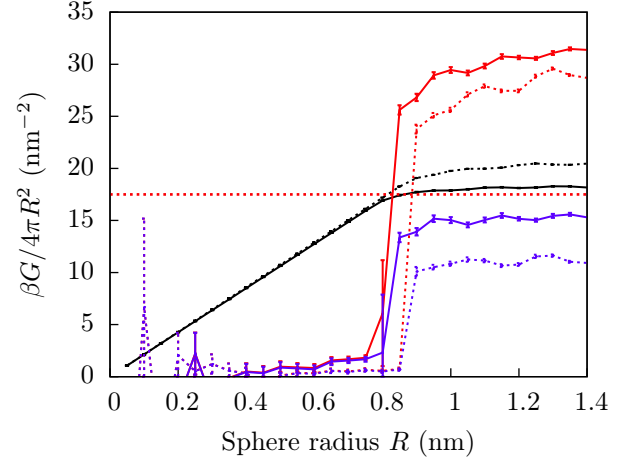

FIG. 11. Solvation free energies G of spheres in the model of Ref. 14 (black), for cell sizes $\lambda = 2.1\,\text{Å}$ (solid) and $\lambda = 2.3\,\text{Å}$ (dashes). The use of the Ising Hamiltonian causes the average value of $H_{\text{large}}[\{n_i\}]$ (red) to significantly exceed the solvation free energy, but also leads to large excess entropies (blue, $TS = \langle H \rangle - G$). At $\lambda = 2.1\,\text{Å}$, but not at $\lambda = 2.3\,\text{Å}$, a fortuitous cancellation leads to correct solvation free energies.

claimed, $\langle H_{\text{large}}[\{n_i\}]\rangle$ is much larger than it should be, but for $\lambda = 2.1\,\text{Å}$, the excess entropy resulting from the unphysical degeneracies of the Ising Hamiltonian exactly cancels this excess energy. This fortuitous cancellation does not occur for different cell sizes, and will not, in general, hold for solutes of different geometries.

[1] W. Kauzmann, Adv. Protein Chem. **14**, 1 (1959).
[2] C. Tanford, *The hydrophobic effect: formation of micelles and biological membranes* (Wiley, 1973).
[3] B. Alberts, A. Johnson, J. Lewis, M. Raff, K. Roberts, and P. Walter, *Molecular Biology of the Cell*, 5th ed. (Garland Science, 2007).
[4] D. Chandler, Nature **437**, 640 (2005).
[5] N. Chennamsetty, V. Voynov, V. Kayser, B. Helk, and B. L. Trout, Proc. Natl. Acad. Sci. U.S.A. **106**, 11937 (2009).
[6] N. Chennamsetty, V. Voynov, V. Kayser, B. Helk, and B. L. Trout, J. Phys. Chem. B **114**, 6614 (2010).
[7] H. Acharya, S. Vembanur, S. N. Jamadagni, and S. Garde, Faraday Discuss. **146**, 1 (2010).
[8] M. R. Shirts, J. W. Pitera, W. C. Swope, and V. S. Pande, J. Chem. Phys. **119**, 5740 (2003).
[9] M. R. Shirts and V. S. Pande, J. Chem. Phys. **122**, 134508 (2005).
[10] W. C. Still, A. Tempczyk, R. C. Hawley, and T. Hendrickson, J. Am. Chem. Soc. **112**, 6127 (1990).
[11] D. Qiu, P. S. Shenkin, F. P. Hollinger, and W. C. Still, J. Phys. Chem. A **101**, 3005 (1997).
[12] K. Lum, D. Chandler, and J. D. Weeks, J. Phys. Chem. B **103**, 4570 (1999).
[13] P. R. ten Wolde, S. X. Sun, and D. Chandler, Phys. Rev. E **65**, 011201 (2001).
[14] P. R. ten Wolde and D. Chandler, Proc. Natl. Acad. Sci. U.S.A. **99**, 6539 (2002).
[15] D. Chandler, *Introduction to Modern Statistical Mechanics* (Oxford University Press, 1987).
[16] B. Roux and T. Simonson, Biophys. Chem. **78**, 1 (1999).
[17] For reduced classes of solutes, such as linear alkanes, surface-area scaling is nonetheless observed. These molecules are properly in the small length-scale regime, where solvation free en-

ergy scales as volume. However, for linear molecules, surface area also scales as volume, leading to the misleading scaling behavior.[4] Moreover, the resulting empirical surface tension is almost negligibly small. Typical values are in the 5–10 cal/mol/$\text{Å}^2 \approx 1\,k_BT/\text{nm}^2$ range,[11,39] in contrast to the water-air surface tension of about $17\,k_BT/\text{nm}^2$ and the water-oil surface tension of about $12\,k_BT\,\text{nm}^2$: see Ref. 18.

[18] C. Tanford, Proc. Natl. Acad. Sci. U.S.A. **76**, 4175 (1979).

[19] D. Huang, P. L. Geissler, and D. Chandler, J. Phys. Chem. B **105**, 6704 (2001).

[20] R. M. Levy, L. Y. Zhang, E. Gallicchio, and A. K. Felts, J. Am. Chem. Soc. **125**, 9523 (2003).

[21] J. Chen and C. L. Brooks, J. Am. Chem. Soc. **129**, 2444 (2007).

[22] A. Wallqvist and B. J. Berne, J. Phys. Chem. **99**, 2893 (1995).

[23] K. Lum and A. Luzar, Phys. Rev. E **56**, R6283 (1997).

[24] P. G. Bolhuis and D. Chandler, J. Chem. Phys. **113**, 8154 (2000).

[25] A. Anishkin and S. Sukharev, Biophys. J. **86**, 2883 (2004).

[26] P. Liu, X. Huang, R. Zhou, and B. J. Berne, Nature **437**, 159 (2005).

[27] T. F. Miller, E. Vanden-Eijnden, and D. Chandler, Proc. Natl. Acad. Sci. U.S.A. **104**, 14559 (2007).

[28] M. V. Athawale, G. Goel, T. Ghosh, T. M. Truskett, and S. Garde, Proc. Natl. Acad. Sci. U.S.A. **104**, 733 (2007).

[29] J. C. Rasaiah, S. Garde, and G. Hummer, Annu. Rev. Phys. Chem. **59**, 713 (2008).

[30] S. N. Jamadagni, R. Godawat, J. S. Dordick, and S. Garde, J. Phys. Chem. B **113**, 4093 (2009).

[31] B. J. Berne, J. D. Weeks, and R. Zhou, Annu. Rev. Phys. Chem. **60**, 85 (2009).

[32] A. J. Patel, P. Varilly, and D. Chandler, J. Phys. Chem. B **114**, 1632 (2010).

[33] G. Hummer, S. Garde, A. E. García, A. Pohorille, and L. R. Pratt, Proc. Natl. Acad. Sci. U.S.A. **93**, 8951 (1996).

[34] See, for instance, D. Huang and D. Chandler, Phys. Rev. E **61**, 1501 (2000) and Refs. 35, 32 and 36.

[36] S. Garde, R. Khare, and G. Hummer, J. Chem. Phys. **112**, 1574 (2000).

[36] L. Xu and V. Molinero, J. Phys. Chem. B **114**, 7320 (2010).

[37] R. Zhou, Proteins **53**, 148 (2003).

[38] I. Daidone, M. B. Ulmschneider, A. Di Nola, A. Amadei, and J. C. Smith, Proc. Natl. Acad. Sci. U.S.A. **104**, 15230 (2007).

[39] J. Chen, C. L. B. III, and J. Khandogin, Curr. Opin. Struc. Biol. **18**, 140 (2008).

[40] C. Y. Janda, J. Li, C. Oubridge, H. Hernandez, C. V. Robinson, and K. Nagai, Nature **465**, 507 (2010).

[41] S. F. Harris, A. K. Shiau, and D. A. Agard, Structure **12**, 1087 (2004).

[42] D. Chandler, Phys. Rev. E **48**, 2898 (1993).

[43] G. Crooks and D. Chandler, Phys. Rev. E **56**, 4217 (1997).

[44] K. Lum, *Hydrophobicity at Small and Large Length Scales*, Ph.D. thesis, University of California, Berkeley (1998), Figure (3.6), page 61.

[45] A. P. Willard and D. Chandler, J. Phys. Chem. B **112**, 6187 (2008).

[46] J. D. Weeks, Annu. Rev. Phys. Chem. **53**, 533 (2002).

[47] J. D. Weeks, R. L. B. Selinger, and J. Q. Broughton, Phys. Rev. Lett. **75**, 2694 (1995).

[48] J. D. Weeks, K. Vollmayr, and K. Katsov, Physica A **244**, 461 (1997).

[49] J. D. Weeks, K. Katsov, and K. Vollmayr, Phys. Rev. Lett. **81**, 4400 (1998).

[50] K. Katsov and J. D. Weeks, J. Phys. Chem. B **105**, 6738 (2001).

[51] H. Berendsen, J. Grigera, and T. Straatsma, J. Phys. Chem. **91**, 6269 (1987).

[52] D. M. Huang and D. Chandler, J. Phys. Chem. B **106**, 2047 (2002).

[53] E. Lemmon, M. McLinden, and D. Friend, in *NIST Chemistry WebBook, NIST Standard Reference Database Number 69*, edited by P. Linstrom and W. Mallard (National Institute of Standards and Technology, Gaithersburg MD, 20899, 2009) http://webbook.nist.gov (retrieved October 25, 2009).

[54] A. H. Narten and H. A. Levy, J. Chem. Phys. **55**, 2263 (1971).

[55] D. M. Huang and D. Chandler, Proc. Natl. Acad. Sci. U.S.A. **97**, 8324 (2000).

[56] A. Pohorille, C. Jarzynski, and C. Chipot, J. Phys. Chem. B **114**, 10235 (2010).

[57] C. H. Bennett, J. Comp. Phys. **22**, 245 (1976).

[58] B. Hess, C. Kutzner, D. van der Spoel, and E. Lindahl, J. Chem. Theory Comput. **4**, 435 (2008).

[59] C. G. Sztrum-Vartash and E. Rabani, J. Phys. Chem. C **114**, 11040 (2010).

[60] J. Chen and C. L. Brooks III, Phys. Chem. Chem. Phys. **10**, 471 (2008).

[61] W. Humphrey, A. Dalke, and K. Schulten, J. Mol. Graphics **14**, 33 (1996). VMD was developed by the Theoretical and Computational Biophysics Group in the Beckman Institute for Advanced Science and Technology at the University of Illinois at Urbana-Champaign.

[62] The parameters of the solute-solute Lennard-Jones potential are those of Ref. 63: $\sigma = 3.905\,\text{Å}$ and $\epsilon = 0.118\,\text{kcal/mol}$. Lorentz-Berthelot mixing rules were used to obtain the water-solute interaction parameters.

[63] W. L. Jorgensen, J. D. Madura, and C. J. Swenson, J. Am. Chem. Soc. **106**, 6638 (1984).

[64] J. D. Weeks, D. Chandler, and H. C. Andersen, J. Chem. Phys. **54**, 5237 (1971).

[65] J.-P. Hansen and I. R. McDonald, *Theory of Simple Liquids*, 3rd ed. (Academic Press, 2006), Section 5.3

[66] L. Verlet and J.-J. Weis, Phys. Rev. A **5**, 939 (1972).

[67] F. Wang and D. Landau, Phys. Rev. Lett. **86**, 2050 (2001).

[68] D. Earl and M. Deem, Phys. Chem. Chem. Phys. **7**, 3910 (2005).

[69] M. R. Shirts and J. D. Chodera, J. Chem. Phys. **129**, 124105 (2008).

[70] S. Plimpton, J. Comp. Phys. **117**, 1 (1995), available at http://lammps.sandia.gov.

[71] See Supplementary Material Document No. NNNN for a listing of the model plate's coordinates, tabulated values of χ_{ab} for water at ambient conditions, and additional $P_V(N)$ distributions.

[72] J. Mittal and G. Hummer, Proc. Natl. Acad. Sci. U.S.A. **105**, 20130 (2008).

[73] R. Godawat, S. N. Jamadagni, and S. Garde, Proc. Natl. Acad. Sci. U.S.A. **106**, 15119 (2009).

[74] S. Sarupria and S. Garde, Phys. Rev. Lett. **103**, 037803 (2009).

[75] J. Mittal and G. Hummer, Faraday Discuss. **146**, 341 (2010).

[76] P. Setny and M. Zacharias, J. Phys. Chem. B **114**, 8667 (2010).

[77] V. Molinero and E. B. Moore, J. Phys. Chem. B **113**, 4008 (2009).

[78] X. Song, D. Chandler, and R. A. Marcus, J. Phys. Chem. **100**, 11954 (1996).

[79] X. Song and D. Chandler, J. Chem. Phys. **108**, 2594 (1998).

[80] M. Doi and S. F. Edwards, *The theory of polymer dynamics* (Oxford, 1988).

[81] N. Kikuchi, A. Gent, and J. Yeomans, Eur. Phys. J. E **9**, 63 (2002).

[82] S. Whitelam, E. H. Feng, M. F. Hagan, and P. L. Geissler, Soft Matter **5**, 1251 (2009).

[83] A. Malevanets and R. Kapral, Europhys. Lett. **44**, 552 (1998).

[84] N. K. Voulgarakis and J.-W. Chu, J. Chem. Phys. **130**, 134111 (2009).

[85] S. Chen and G. D. Doolen, Ann. Rev. Fluid Mech. **30**, 329 (1998).

[86] In Ref. 13, the term proportional to n_i is omitted. Since $\phi(\mathbf{r})$ only acts on cells with $n_i = 1$, this omission is inconsequential, and shows up as an extra factor of 2 in their value of a.

[87] J. S. Rowlinson and B. Widom, *Molecule Theory of Capillarity* (Dover, 1982). Chapter 3.

[88] J. D. Weeks, J. Chem. Phys. **67**, 3106 (1977).

[89] C. Vega and E. de Miguel, J. Chem. Phys. **126**, 154707 (2007).

[90] W. E. Lorensen and H. E. Cline, SIGGRAPH Comput. Graph. **21**, 163 (1987).

[91] C. B. Haselgrove, Math. Comput. **15**, 323 (1961).

[92] H. Conroy, J. Chem. Phys. **47**, 5307 (1967).